Accelerating Fluid Dynamics Problems in Planet Formation with Machine Learning

by

Shunyuan Mao
B.Sc., University of Science and Technology of China, 2019
M.Sc., University of Victoria, 2022

A Dissertation Submitted in Partial Fulfillment of the
Requirements for the Degree of

DOCTOR OF PHILOSOPHY

in the Department of Physics and Astronomy

Accelerating Fluid Dynamics Problems in Planet Formation with Machine Learning

by

Shunyuan Mao
B.Sc., University of Science and Technology of China, 2019
M.Sc., University of Victoria, 2022

Supervisory Committee

Dr. Ruobing Dong, Supervisor
(Department of Physics and Astronomy)

Dr. Lu Lu, Outside Member
(Department of Statistics and Data Science, Yale University)

Dr. Paris Perdikaris, Outside Member
(Department of Mechanical Engineering and Applied Mechanics, University of Pennsylvania)

ABSTRACT

I develop two machine learning tools for solving forward and inverse problems in protoplanetary disks. The first tool, Protoplanetary Disk Operator Network (PPDONet), predicts the solution of disk–planet interactions in real–time. PPDONet is based on Deep Operator Networks (DeepONets), a class of neural networks capable of learning non–linear operators to represent deterministic and stochastic differential equations. It maps three scalar parameters in a disk–planet system – the Shakura & Sunyaev viscosity α, the disk aspect ratio h_0, and the planet–star mass ratio q – to steady–state solutions of the disk surface density, radial velocity, and azimuthal velocity. Comprehensive testing demonstrates the accuracy of PPDONet, with predictions for one system made in less than a second on a laptop. A public implementation of PPDONet is available at `https://github.com/smao-astro/PPDONet`.

The second tool, Disk2Planet, infers key parameters in disk-planet systems from observed disk structures. It processes two-dimensional density and velocity maps to output the Shakura–Sunyaev viscosity, disk aspect ratio, planet–star mass ratio, and the planet's location. Disk2Planet integrates the Covariance Matrix Adaptation Evolution Strategy (CMA-ES), an evolutionary algorithm for complex optimization problems, with PPDONet. Fully automated, Disk2Planet retrieves parameters within three minutes on an Nvidia A100 GPU, achieving accuracies ranging from thousandths to percentages. It effectively handles data with missing parts and unknown levels of noise.

Together, these tools advance the field of planet formation by providing rapid, accurate solutions and parameter inferences for disk-planet systems, enhancing our understanding of the underlying physics of protoplanetary disks.

Contents

List of Tables

List of Figures

ACKNOWLEDGEMENTS

I would like to thank:

- my advisor, Dr. Ruobing Dong for his invaluable guidance, support, and encouragement throughout my research.
- my collaborator, Dr. Kwang Moo Yi, Dr. Lu Lu, Dr Sifan Wang, Dr. Paris Perdikaris for their insightful discussions to the development of the projects.
- my colleague, Dr. Weiqi Wang for his assistance in the experiments.
- Xuening Bai, Pablo Benítez-Llambay, Shengze Cai, Miles Cranmer, Bin Dong, Xiaotian Gao, Jiequn Han, Pinaghui Huang, Xiaowei Jin, Hui Li, Tie-Yan Liu, Chris Ormel, Wenlei Shi, Karun Thanjavur, Yiwei Wang, Yinhao Wu, Zhenghao Xu, Minhao Zhang, and Wei Zhu for help and useful discussions in the projects.
- Natural Sciences and Engineering Research Council of Canada (NSERC), Digital Research Alliance of Canada, the Alfred P. Sloan Foundation, and the Government of Canada's New Frontiers in Research Fund (NFRF), [NFRFE-2022-00159] for their support to the projects.

DEDICATION

To my parents and friends, for their endless support and encouragement.

Chapter 1

Introduction

Planets form in protoplanetary disks, which are flattened, gaseous disks surrounding newborn stars [Andrews, 2020]. To study planet formation in the outer disk beyond the snowline, a straightforward approach is to directly image the forming planets in these disks [e.g., Keppler et al., 2018, Müller et al., 2018, Wagner et al., 2018, Christiaens et al., 2019, Haffert et al., 2019, Hashimoto et al., 2020, Wang et al., 2020, Currie et al., 2022, Zhou et al., 2022]. Successful detections can provide critical information about the process, such as the mass and orbit of the forming planets. However, this approach is challenging with current observational techniques as the signals from the stars and disks overwhelm those from the planets [Currie et al., 2022]. These factors severely limit our understanding of how planets form.

To detect young planets embedded in protoplanetary disks, an alternative method is to infer their presence and constrain their parameters from observations of large-scale disk structures produced by disk-planet interactions [Paardekooper et al., 2022]. The morphology of these structures, such as gaps [e.g., Paardekooper and Mellema, 2006, Rosotti et al., 2016, Dipierro and Laibe, 2017], spiral arms [e.g., Bae and Zhu, 2018, Dong et al., 2015a], vortices [e.g., Zhu et al., 2014], and kinematic perturbations [e.g., Pinte et al., 2018, Teague et al., 2018, Izquierdo et al., 2021, Rabago and Zhu, 2021], depends on the properties of the disk and the planets, such as the viscosity and aspect ratio of the disk, and the masses and orbits of the planets.

Deriving planetary parameters from observed disk structures requires solving *the inverse problem*: deducing causes from observed effects. It involves fitting observations with parametrized disk-planet models predicted by a *forward problem solver*, which calculates the effects from the causes. The process iteratively fine-tunes parameters to achieve a satisfactory fit to the observed data.

Conventional inverse problem solvers, as illustrated in Fig. 1.1, are both computationally and labor-intensive. The forward problem solver relies on numerical simulations, each demanding substantial computational resources [e.g., Cilibrasi et al., 2023]. This demand is multiplied by the number of iterations needed to process a single observed system [e.g., Dipierro et al., 2015, Dong et al., 2015b, Jin et al., 2016, Pinte et al., 2019]. Additionally, the procedure requires significant expert involvement for the initial setup, continuous monitoring, and adjustments of simulations. As the discovery of structures in disks accelerates — with over 100 disks newly resolved in a regular year [Benisty et al., 2022] — the demand to fit all disk observations through simulations vastly outstrips the available computational and human resources.

The high computational cost spurs the development of alternative approaches, such as direct mapping of planet–induced structures to parameters in disk–planet systems without numerical simulations. Initially, this mapping involved using empirical formulas to correlate a small number of (or a single) scalar observable metrics of disk structures, such as gap width or depth, to system parameters [e.g., Dong et al., 2018, Zhang et al., 2018, Dong and Fung, 2017]. However, these approaches rely solely on a limited number of scalar metrics, failing to encapsulate the rich information in images, resulting in degeneracies and large uncertainties in the results (e.g., Fung et al. 2014).

To address these limitations, Convolutional Neural Networks (CNNs) [O'Shea and Nash, 2015, Li et al., 2021] are employed in several pioneering works to map entire images to disk and planet parameters [Auddy et al., 2021, Zhang et al., 2022, Terry et al., 2022, Ruzza et al., 2024]. The CNNs establish the relationships between disk density maps ("effects") and system parameters ("causes") by training on simulated data where both are known. These networks analyze spatial correlations among pixel values to identify the characteristics of planet-induced disk structures, leveraging the comprehensive information in an image rather than relying on a limited array of highly synthesized scalar metrics (e.g., gap width). This method not only improves inference accuracy but also streamlines the process of retrieving planet parameters from disk observations for end users by (1) obviating the need for numerical simulations and (2) circumventing the tedious iterative fitting process.

However, the accuracy of parameters retrieved by CNN-based inverse problem solvers typically only reaches the tenths place. Furthermore, such accuracy is assured solely for images within the training data distribution and may significantly deteriorate when applied to real observations, which may not conform to this distribution.

This challenge is particularly pronounced in images (1) with noise [Ruzza et al., 2024, §5.3], as the noise level in actual observations is measured only afterward and varies from one observation to another, challenging the preparation of the training dataset; and (2) with missing parts, e.g., due to foreground absorption (Bruderer et al. 2014, Fig. 1; Tsukagoshi et al. 2019). These scenarios underscore the inherent difficulties in applying CNN-based solvers to real observations.

To address the aforementioned challenges, I have developed two complementary machine learning-based tools: a forward problem solver named PPDONet, and an inverse problem solver called Disk2Planet.

PPDONet can instantaneously predict the steady-state disk structure in both surface density and velocities of a disk-planet system. The forward problem solver is based on a recent architecture, DeepONets [Lu et al., 2021], that greatly reduces the computing cost of simulating physical systems. In particular, they learn non-linear operators that represent deterministic and stochastic differential equations. They can predict solutions for differential equations with parametric boundary conditions, initial conditions, or forcing terms. As a result, they provide better generalization and faster convergence with respect to the volume of training data [Lu et al., 2021].

I train DeepONets (§2.2) with hydrodynamic simulations produced using numerical solvers and test the networks by reproducing empirical relationships in disk-planet interactions (§2.3). This tool, PPDONet, is publicly available on GitHub[1] under a GPL v3.0 License and version 0.1.0 is archived in Zenodo [Mao, 2023]. A web interface[2] has been developed for the convenience of usage as well.

Disk2Planet is a fast and fully automated inverse problem solver that can infer planet and disk parameters from observed disk structures with high levels of accuracy and robustness. On average, it takes three minutes on an Nvidia A100 graphics processing unit (GPU) to process one system with a single image as the input. Disk2Planet adopts the framework of the iterative parameter update approach (Fig. 1.1), but replaces the slow and expensive numerical simulations with a fast machine learning–based forward problem solver, PPDONet, introduced by Mao et al. 2023. Additionally, the tool employs the Covariance Matrix Adaptation Evolution Strategy [Hansen, 2006, 2009, Hansen et al., 2010, 2019, CMA–ES] to optimize parameter updates in iterations, thus freeing humans from interactions. The tool can handle images with unknown noise levels, with missing parts of arbitrary shapes, and

[1]PPDONet codebase: `https://github.com/smao-astro/PPDONet`

[2]Web app: `https://ppdonet-1.herokuapp.com`

in various combinations of density and/or velocities. Disk2Planet achieves percentile to thousandth–level accuracy in inferred parameters for the first time.

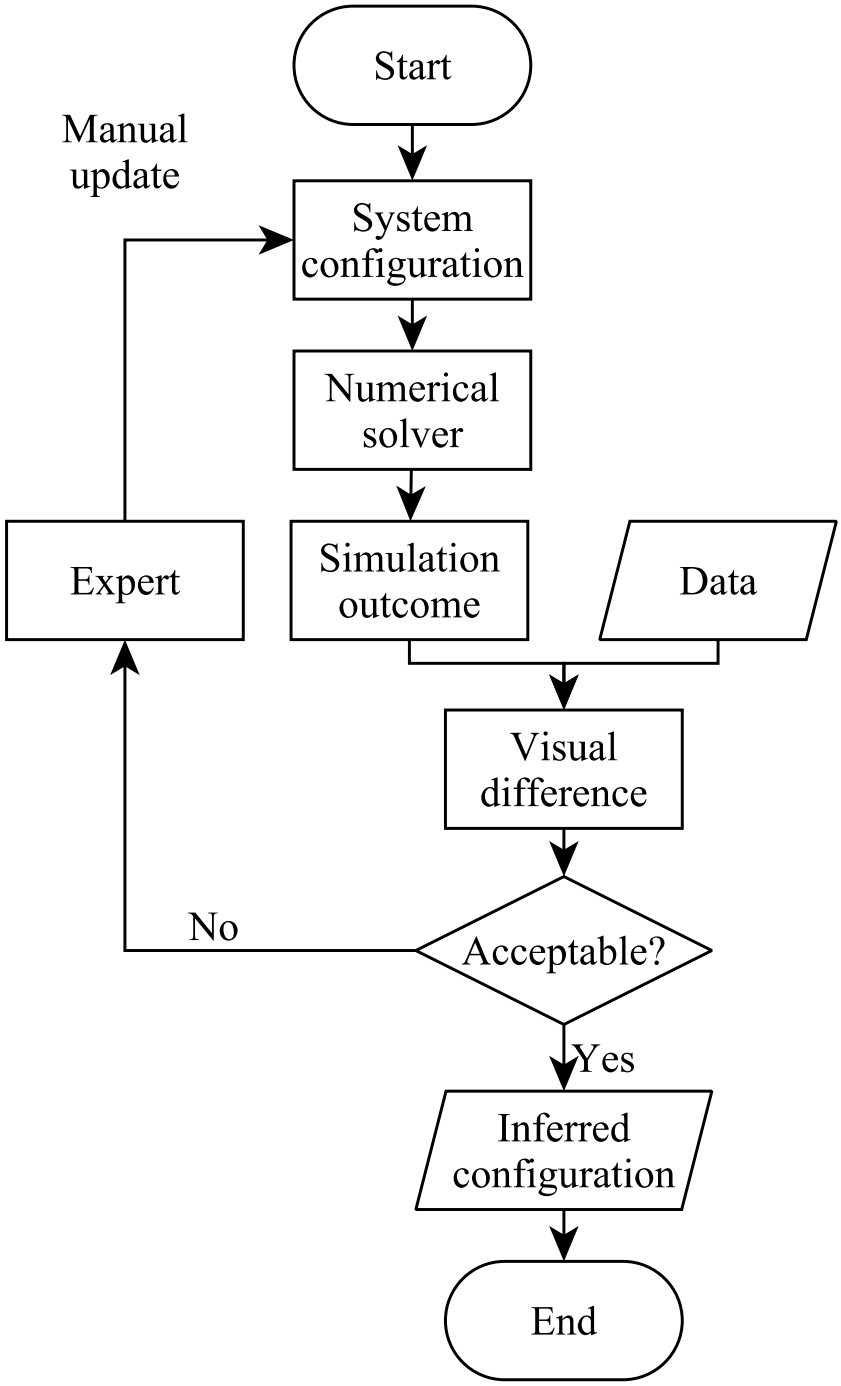

Figure 1.1: The framework of conventional inverse problem solvers. Each iteration begins with an estimation of the system configuration, which includes parameters in a disk-planet system. This configuration is sent to a numerical solver to generate the resulting disk maps. Expert analysis then evaluates the visual discrepancies between the simulation outcomes and the observational data, leading to iterative refinements of the system parameters.

Chapter 2

PPDONet: Deep Operator Networks for Fast Prediction of Steady-State Solutions in Disk-Planet Systems

2.1 DeepONets

As my work utilizes the DeepONet [Lu et al., 2021] architecture, I first review DeepONet. DeepONet is a machine learning-based approach that utilizes a neural network to approximate a mathematical operator denoted as G. In disk-planet systems, G maps a set of scalar parameters, $\vec{p}$, to a distribution function, $G(\vec{p})$, that can be evaluated at any desired location. Specifically, in my networks $\vec{p}$ includes the Shakura & Sunyaev viscosity α, the disk aspect ratio h_0, and the planet-star mass ratio q, and $G(\vec{p})\,(r,\theta)$ represents the surface density or velocity at a specified point (r,θ). Therefore, the DeepONet architecture comprises two kinds of inputs: scalar parameters, $\vec{p}$, and coordinates (r,θ), and one output, which can be either surface density, radial velocity, or azimuthal velocity.

Figure 2.1 depicts the architecture of PPDONet. To map inputs $(\vec{p})$ to solutions $(G(\vec{p}))$, the scalar parameters are encoded by a subnetwork referred to as the "branch network." This network is fully connected and consists of four 100-neuron hidden layers (4×100). Concurrently, the coordinate inputs are encoded by another fully connected subnetwork, the "trunk network," which has five layers of 256 neurons

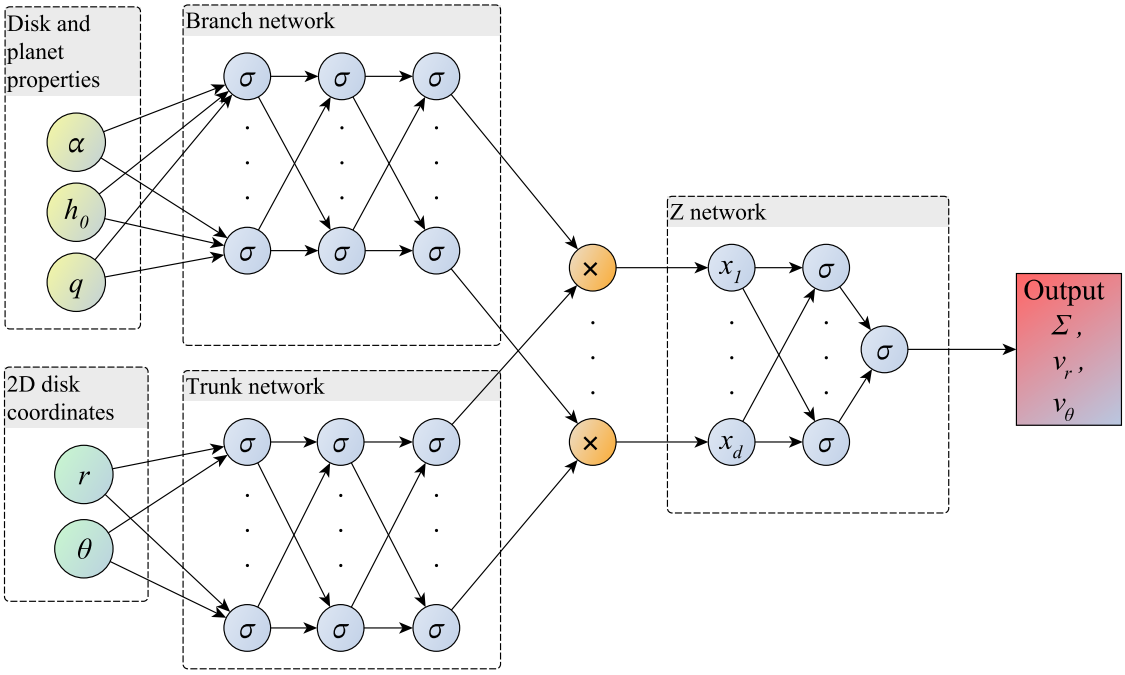

Figure 2.1: PPDONet architecture used in this work. A fully connected subnetwork, called "branch network", encodes scalar parameters, the disk and planet properties, while another fully connected subnetwork, called "trunk network", encodes the coordinates. I produce the inputs x_i, $i = 1, ..., d$, $d = 50$, for the third network ("Z network") by element-wise multiplication of the outputs from the branch and trunk networks. The Z network is a fully connected single-hidden-layer network whose output represents surface density or velocity. The σ in blue nodes are neurons in layers.

each. I obtain the inputs x_i, $i = 1, ..., d$, $d = 50$, for the third network ("Z network" in Figure 2.1) by element-wise multiplication of the outputs from the branch and trunk networks. The Z network is a fully connected single-hidden-layer network whose output represents surface density or velocity. I employ the self-scalable Tanh activation function (Stan) [Gnanasambandam et al., 2022] for fitting surface density and azimuthal velocity, as it enables fast convergence and results in small training and testing errors; however, the Tanh activation function outperforms Stan for learning radial velocity.

2.2 Implementation

2.2.1 Hydrodynamic simulations for training, validating, and testing neural networks

I focus on large-scale structures, such as gaps and spiral arms, induced by a single planet on a fixed circular orbit in gaseous disks. The disk's initial profiles are described by the equations:

$$\Sigma = \Sigma_0 \left(r/r_{\rm p}\right)^{-1/2}, \tag{2.1a}$$

$$v_r = -\frac{3}{2}\alpha {h_0}^2 \sqrt{\frac{GM_\odot\left(1+q\right)}{r}}, \tag{2.1b}$$

$$v_\theta = \sqrt{1-\frac{3}{2}{h_0}^2}\sqrt{\frac{GM_\odot\left(1+q\right)}{r}}, \tag{2.1c}$$

where Σ is the surface density, v_r is the radial velocity, v_θ is the azimuthal velocity, α is the Shakura & Sunyaev viscosity, and h_0 is the disk aspect ratio. Both α and h_0 are kept constant throughout the disk. The models are developed for a fixed initial radial surface density profile and a radially constant disk aspect ratio. The planet is at $r = r_{\rm p}$ with mass $m_{\rm p} = qM_\odot$. The initial surface density at $r_{\rm p}$ is $\Sigma_0 = 1$. This setup ensures my model corresponds to planet-free steady-state accretion disks [Fung et al., 2014]. The boundary conditions are fixed and determined by initial values, which ensure a constant mass inflow [Fung et al., 2014].

Table 2.1: Disk and planet parameter space

Parameter	Minimum	Maximum
α	3×10^{-4}	0.1
h_0	0.05	0.1
q	5×10^{-5}	2×10^{-3}

The outcomes of disk-planet interaction in my simulations are determined by three parameters: α, h_0, and q. Massive planets open deep gaps, while large viscosity and aspect ratio hinder the opening of deep gaps. With $q > 2 \times 10^{-3}$, or $\alpha < 3 \times 10^{-4}$, a disk may develop vortices or other asymmetric and time-varying structures [Fung et al., 2014]. In this work, I only focus on disks capable of reaching a steady state with parameters bounded by Table 2.1.

To collect data for training neural networks, choose the best ML models, and test their performance on unseen parameters, I generate 768 FARGO3D [Masset, 2000, Benítez-Llambay and Masset, 2016] hydrodynamic simulations with $r \times \theta = 381 \times 1143$ resolution. I sample α, h_0, and q from Sobol sequences [Sobol', 1967], quasi-random low-discrepancy sequences effective in generating inputs for machine learning tasks [Wu et al., 2023]. I divide the 768 FARGO3D simulations into three groups with 448, 64, and 256 cases for training, validation, and testing, respectively. In training, I compare neural network predictions with simulations to formalize loss functions. In testing, I measure errors on unseen simulations to assess the generalization of my neural networks. All simulations are run for $0.314\tau_\nu$ to reach (quasi) steady state, where τ_ν is the disk viscous timescale

$$\tau_\nu \approx \frac{r_\mathrm{p}^2}{\nu} = \frac{1}{\alpha c_\mathrm{s} h} = \frac{1}{\alpha {h_0}^2}. \tag{2.2}$$

2.2.2 Network training

To fit the steady-state solution of three quantities – surface density Σ, radial velocity v_r, and azimuthal velocity v_θ – I train three separate neural networks. As some of the inputs span several orders of magnitude, I convert them to logarithmic scales. I then normalize both the scalar parameters and coordinate inputs. To facilitate learning, I perform two additional steps: 1) I take the logarithm of the surface density, and 2) I subtract the background from the radial and azimuthal velocities. As a result, my loss function for surface density is

$$L_\Sigma = \frac{1}{N} \sum_{i=1}^{N} \left[\log(\Sigma_i^\mathrm{pred}) - \log(\Sigma_i^\mathrm{truth}) \right]^2, \tag{2.3}$$

while my loss functions for velocities are

$$L_{v_r} = \frac{1}{N} \sum_{i=1}^{N} \left[{v_r}_i^\mathrm{pred} - {v_r}_i^\mathrm{truth} \right]^2 \tag{2.4}$$

and

$$L_{v_\theta} = \frac{1}{N} \sum_{i=1}^{N} \left[{v_\theta}_i^\mathrm{pred} - {v_\theta}_i^\mathrm{truth} \right]^2. \tag{2.5}$$

The indices i go through all the grid points in all the simulations in a training batch [1]. I regard FARGO3D outputs as "ground truth", and use the superscript $^{\text{truth}}$ for them. Superscript $^{\text{pred}}$ is for neural network predictions. The hyperparameters used in my networks and training processes are listed in Table 2.2.

Table 2.2: Machine learning hyperparameters

Hyper-parameter	Default value
Training data size	448
Validation data size	64
Testing data size	256
Batch size	32
Num. steps for each batch	3
Initialization	Glorot normal[A]
Learning rate	0.0005
Learning rate decay rate	0.9
Learning rate transition steps	2000
Optimizer	Adam[B]
Total number of iterations	10^5
Branch network layer size	100, 100, 100, 100, 50
Trunk network layer size	256, 256, 256, 256, 256, 50
Z network layer size	100, 1

[A] Glorot and Bengio [2010]
[B] Kingma and Ba [2014]

2.3 Tests

I present a series of tests. In §2.3.1, I compare the 2D maps of predicted surface density and velocity with the ground truth generated by FARGO3D. Then I compare the predicted gap profile to the true profile in §2.3.2. I further examine the behavior of my prediction on groups of disks by reproducing several empirical relationships from previous works in §2.3.3.

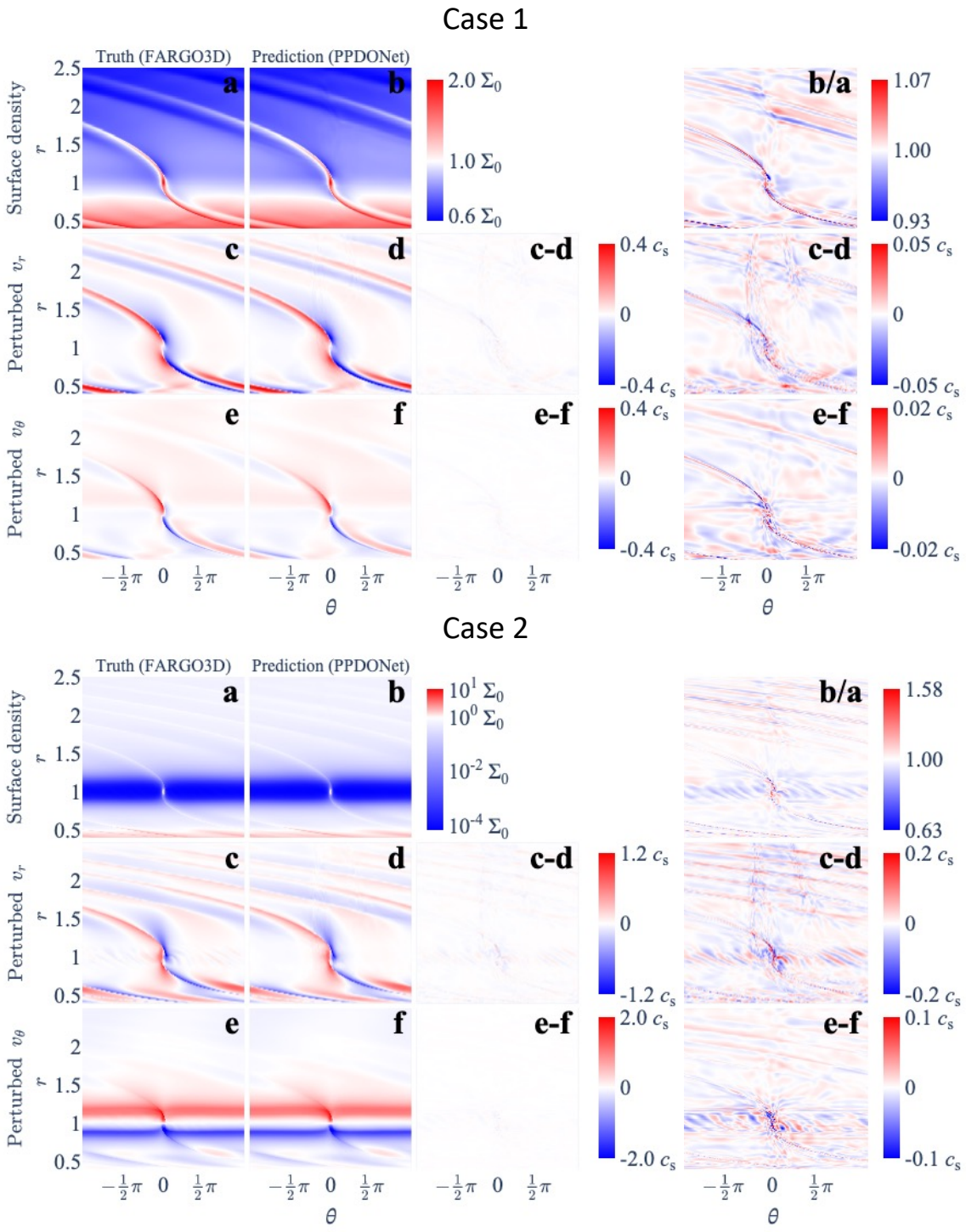

Figure 2.2: Two-dimensional comparisons of predicted surface density and velocity distribution. Case 1: $(\alpha, h_0, q) = (0.013, 0.092, 6.0 \times 10^{-4})$. Case 2: $(\alpha, h_0, q) = (5.2 \times 10^{-4}, 0.053, 1.6 \times 10^{-3})$. Left (a, c, and e): Ground truth generated from FARGO3D simulations. Middle (b, d, and f): Neural network predictions. For the two left columns, I subtract the initial value from the two velocities to highlight the perturbations. Two right columns: Differences or ratios. Surface density differences are measured by the ratio $\Sigma^{\rm pred}/\Sigma^{\rm truth}$, so that the gap region is highlighted. Velocity differences are shown in absolute errors.

2.3.1 2D maps of surface density and velocities

Two representative cases are presented in Figure 2.2, highlighting density waves (case 1 with $\alpha = 0.013$, $h_0 = 0.092$, and $q = 6.0\times10^{-4}$) and gaps (case 2 with $\alpha = 5.2\times10^{-4}$, $h_0 = 0.053$, and $q = 1.6 \times 10^{-3}$). The left column shows the ground truth from FARGO3D, the middle column shows the PPDONet predictions, and the two right columns show the differences or ratios between the two. To ease the comparison in the perturbed radial and azimuthal velocity, I subtract their initial values from the corresponding panels. For surface density, I calculate the ratio between the prediction and ground truth to highlight the gap region. For velocities, which can take both positive and negative values, I show absolute errors.

A visual inspection of the model-prediction comparisons (panels a, c, e *vs* b, d, f) shows that the differences in the location and contrast of both density waves and gaps are negligible. This is achieved despite these perturbations' sharp morphology relative to the background.

2.3.2 1D surface density profile

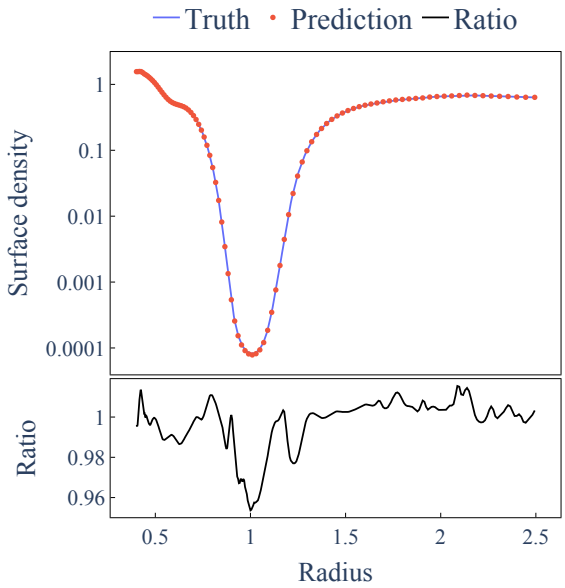

Figure 2.3: Gap profile comparison for one example case with $\alpha = 5.2 \times 10^{-4}$, $h_0 = 0.053$, and $q = 1.6 \times 10^{-3}$. Blue: Ground truth from FARGO3D. Red: PPDONet prediction. Bottom panel: The ratio between the two.

[1]To compare with FARGO3D, the grid points for surface density are cell-centered, while velocities are face-centered [see Benítez-Llambay and Masset, 2016, §2.3]

Gaps are one of the most important disk structures whose profiles are closely related to and can be used to constrain the properties of gap-opening planets [Kanagawa et al., 2016]. I carry out quantitative comparisons between PPDONet predictions and the ground truth by analyzing the azimuthally averaged 1D surface density radial profile of gaps. To measure 1D profiles, I mask regions contaminated by the planet and azimuthally average the surface density. One representative example ($\alpha = 5.2 \times 10^{-4}$, $h_0 = 0.053$, and $q = 1.6 \times 10^{-3}$) is shown in Figure 2.3. The gap profiles from FARGO3D and PPDONet prediction overlap with no noticeable difference, and the ratio between the two deviates from unity by $\sim$1%, indicating an excellent agreement.

2.3.3 Empirical dependence of the morphology of disk structures on disk and planet properties

A few quantitative empirical relationships have been synthesized to connect the properties of disk features produced by planets to the properties of planets and the disk. I examine three such relationships using PPDONet-simulated disks, generated within ten minutes on a laptop.

Gap Depth ($\Sigma_{\rm gap}$). The average surface density inside a gap depends on α, h_0, and q. Fung et al. [2014] simulated 21 disk-planet systems and fitted an empirical relationship when the planet masses were less than five times that of Jupiter:

$$\Sigma_{\rm gap}/\Sigma_0 = 0.14 \left(\frac{q}{0.001}\right)^{-2.16} \left(\frac{\alpha}{0.01}\right)^{1.41} \left(\frac{h_0}{0.05}\right)^{6.61} . \tag{2.6}$$

I measure gap depth in my sample of 500 disk models with the same method as Fung et al. [2014], namely averaging the surface density inside the annulus $|r - r_{\rm p}| < 2\max(R_{\rm H}, h)$, excluding the region $|\phi - \phi_{\rm p}| < 2\max(R_{\rm H}, h)/r_{\rm p}$. I fit the data with a power-law similar to Fung et al. [2014] and measure the standard errors of the estimate, namely standard deviation of the error terms, using IBM SPSS Statistics. I get an adjusted R^2 equaling 0.995, indicating an excellent fit

$$\begin{aligned} \Sigma_{\rm gap}/\Sigma_0 &= 0.13 \pm 0.02 \left(\frac{q}{0.001}\right)^{-2.50\pm0.01} \\ &\times \left(\frac{\alpha}{0.01}\right)^{1.421\pm0.007} \left(\frac{h_0}{0.05}\right)^{7.26\pm0.03} . \end{aligned} \tag{2.7}$$

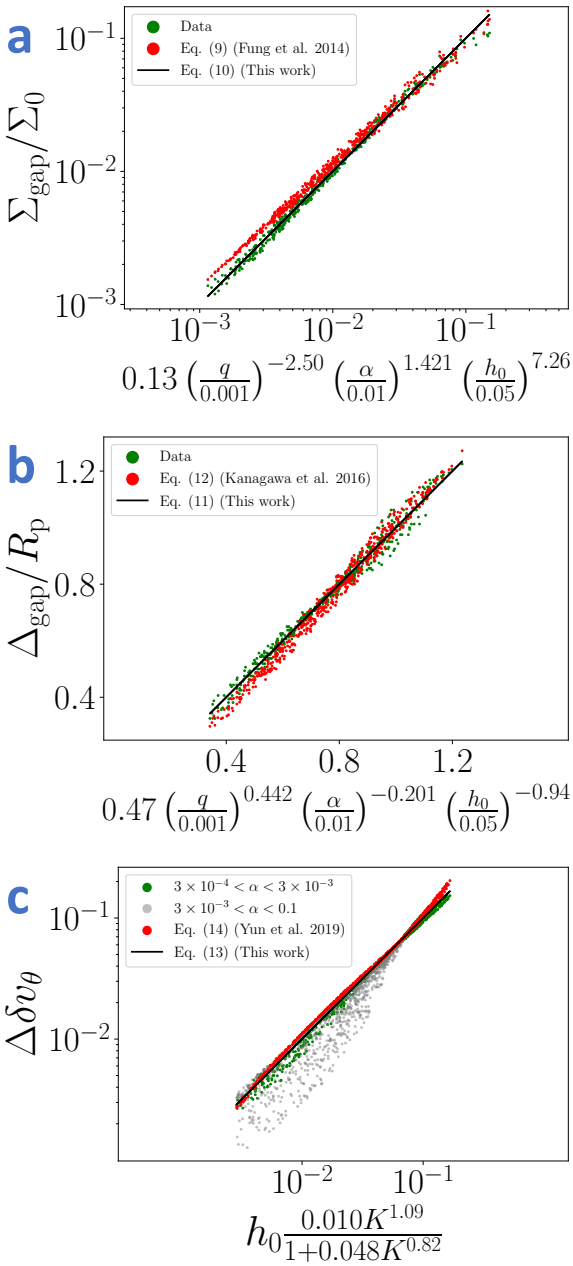

Figure 2.4: Empirical relationships for disk morphology. (a) presents the gap depth $\Sigma_{\rm gap}$ as a function of α, h_0, and q; (b) shows the gap width $\Delta_{\rm gap}$ against α, h_0, and q; and (c) depicts the amplitudes of perturbed rotational velocity $\Delta\delta v_\theta$ against the dimensionless parameter $K \equiv q^2 {h_0}^{-5}\alpha^{-1}$.

Figure 2.4a shows the data, the prediction of Equation (2.6), and my fit. Note that due to the construction of the horizontal axis, the prediction of Equation (2.6) is shown using dots instead of a curve. While the power-law indexes of my fit differ slightly from those of Fung et al. [2014], the two exhibit the same trend: gaps are deeper in disks with lower viscosity and aspect ratio opened by more massive planets. I note that with hundreds of disk models, I are not only able to find a fitting function, but also to constrain the *uncertainties* in the fitted parameters, which are hard to achieve with tens of disk models produced using numerical solvers.

Gap Width ($\Delta_{\rm gap}$) . Gap width also relates to disk and planet properties and is an observable frequently used to constrain planet masses in observations [Kanagawa et al., 2016, Zhang et al., 2018]. I measure the gap width in my sample and examine the empirical relationship in Kanagawa et al. [2016]. I adopt a similar method in measuring $\Delta_{\rm gap}$ as Kanagawa et al. [2016], i.e., the radial separation between the inner and outer gap edges, with the edges identified at 0.5 Σ_0. I fit the data by a power law:

$$\begin{aligned}\Delta_{\rm gap}/R_{\rm p} &= 0.47 \pm 0.04 \left(\frac{q}{0.001}\right)^{0.442\pm0.003} \\ &\times \left(\frac{\alpha}{0.01}\right)^{-0.201\pm0.002} \left(\frac{h_0}{0.05}\right)^{-0.94\pm0.02} .\end{aligned} \tag{2.8}$$

In comparison, Equation (4) in Kanagawa et al. [2016] gives

$$\Delta_{\rm gap}/R_{\rm p} = 0.39 \left(\frac{q}{0.001}\right)^{0.5} \left(\frac{\alpha}{0.01}\right)^{-0.25} \left(\frac{h_0}{0.05}\right)^{-0.75} . \tag{2.9}$$

The two are shown in Figure 2.4b, a reproduction of Figure 3 in Kanagawa et al. [2016], with 19× more data points (500 in my case *vs* 26 in Kanagawa et al. [2016]). Again, the more than one order of magnitude bigger sample size enables me to obtain uncertainties in the fitted parameters.

Azimuthal Velocity Perturbation ($\Delta\delta v_\theta$). I also examine the azimuthally averaged normalized perturbed rotational velocity $v_\theta(r,\theta)$: $\delta v_\theta(r) \equiv \langle (v_\theta(r,\theta) - v_{\theta,0}(r,\theta))\,/v_{\theta,0}(r,\theta)\rangle$, where $v_{\theta,0}(r,\theta)$ is the initial value. I then define the difference between the maximum and minimum $\delta v_\theta(r)$ within a radius range of $r \in (0.5r_{\rm p}, 1.5r_{\rm p})$ as $\Delta\delta v_\theta \equiv$

$\max[\delta v_\theta(r)] - \min[\delta v_\theta(r)]$ [2] [see Yun et al., 2019, Figure 1d]. The measurements are conducted on two datasets each containing 500 disks in different parameter spaces. First, I generate disks from PPDONet with the same range of α as Yun et al. [2019]: $3 \times 10^{-4} < \alpha < 3 \times 10^{-3}$. I measure the perturbed velocity amplitudes in my sample (green dots) following Yun et al. [2019] and obtain the best fit (black line):

$$\Delta\delta v_\theta = h_0 \frac{(0.010 \pm 0.001) K^{1.09 \pm 0.03}}{1 + (0.048 \pm 0.003) K^{0.82 \pm 0.02}}, \tag{2.10}$$

where $K \equiv q^2 {h_0}^{-5} \alpha^{-1}$. This is similar to the one obtained by (red dots) Yun et al. [2019]

$$\Delta\delta v_\theta = h_0 \frac{0.007 K^{1.38}}{1 + 0.06 K^{1.03}}. \tag{2.11}$$

The data and the two fits are shown in Figure 2.4c. Next, I generate disks from PPDONet with larger α, $3 \times 10^{-3} < \alpha < 0.1$, and measure $\Delta\delta v_\theta$ (grey dots). I find neither relationship is suitable for accurately characterizing disks with high viscosity. This is as expected, because when $\alpha \gtrsim 0.01$ viscous damping of density waves strongly affects the evolution of waves and their profiles [Miranda and Rafikov, 2020].

2.4 SUMMARY

I develop a machine learning tool, PPDONet, based on Deep Operator Networks [DeepONets; Lu et al., 2021] to predict the steady-state solutions of disk-planet interactions in parameterized protoplanetary disks. I train PPDONet using 448 disks generated by FARGO3D simulations. The trained operator is able to map three scalar parameters – the Shakura & Sunyaev viscosity α, the disk aspect ratio h_0, and the planet-star mass ratio q – to steady-state solutions of disk surface density, radial velocity, and azimuthal velocity. Currently, PPDONet is the first and only public tool that is able to accomplish this forward problem. It can predict the structures of 500 disk-planet systems in a few minutes on a laptop, many orders of magnitude faster than conventional numerical simulations.

To evaluate the performance of PPDONet, I present a comprehensive set of tests. I compare 2D maps (§2.3.1) and 1D surface density radial profiles (§2.3.2) generated from PPDONet with those produced by FARGO3D simulations. The two are consistent with each other with little noticeable difference. I use PPDONet to generate

[2] The $\Delta\delta v_\theta$ in my work is defined as δ_V in Yun et al. [2019].

multiple samples of disk-planet interaction, each containing on the order of $1,000$ disks, and revisit several empirical relationships previously reported (§2.3.3), including how gap depth, gap width, and azimuthal velocity perturbation depend on α, h_0, and q. Overall, I recover previously found correlations. In addition, thanks to the one to two orders of magnitude larger samples that PPDONet is able to quickly produce compared with those previously produced using conventional numerical solvers, I are able to constrain the uncertainties in the fitting parameters, a nearly impossible task in the past due to small sample sizes.

My tool is positioned to replace conventional numerical simulations in certain applications. It is publicly available at `https://github.com/smao-astro/PPDONet`.

Chapter 3

Disk2Planet: A Robust and Automated Machine Learning Tool For Parameter Inference in Disk–Planet Systems

3.1 Method

The inputs for my inverse problem solver consist of one or a combination of 2D maps of surface density and velocity distributions in a steady–state disk with a planet on a stable circular orbit. The solver is designed to find the optimal set of five parameters — Shakura–Sunyaev viscosity (α), disk aspect ratio (h_0), planet–star mass ratio (q), and planetary location (radius r_p and azimuth θ_p) — that results in the minimal differences between the predicted disk model and the input data. This is accomplished through an iterative process outlined in Fig. 3.1.

In each iteration, I use a 5D Gaussian distribution to represent my current knowledge of (α, h_0, q, r_p, θ_p). The mean of the Gaussian indicates the most probable parameter values. Initially, I sample $4,096$ parameter sets uniformly in the parameter space of interest: $3 \times 10^{-4} \leq \alpha \leq 0.1$, $0.05 \leq h_0 \leq 0.1$, $5 \times 10^{-5} \leq q \leq 2 \times 10^{-3}$, and r_p and θ_p within the input data image's boundaries (50–150 au for r_p and 2π for θ_p, or wherever the truncation due to cropping is; §3.2.4). The mean of the Gaussian is initialized to the parameters with the lowest score (§3.1.2) among the $4,096$ parameter sets. The standard deviation of the Gaussian reflects the confidence in the

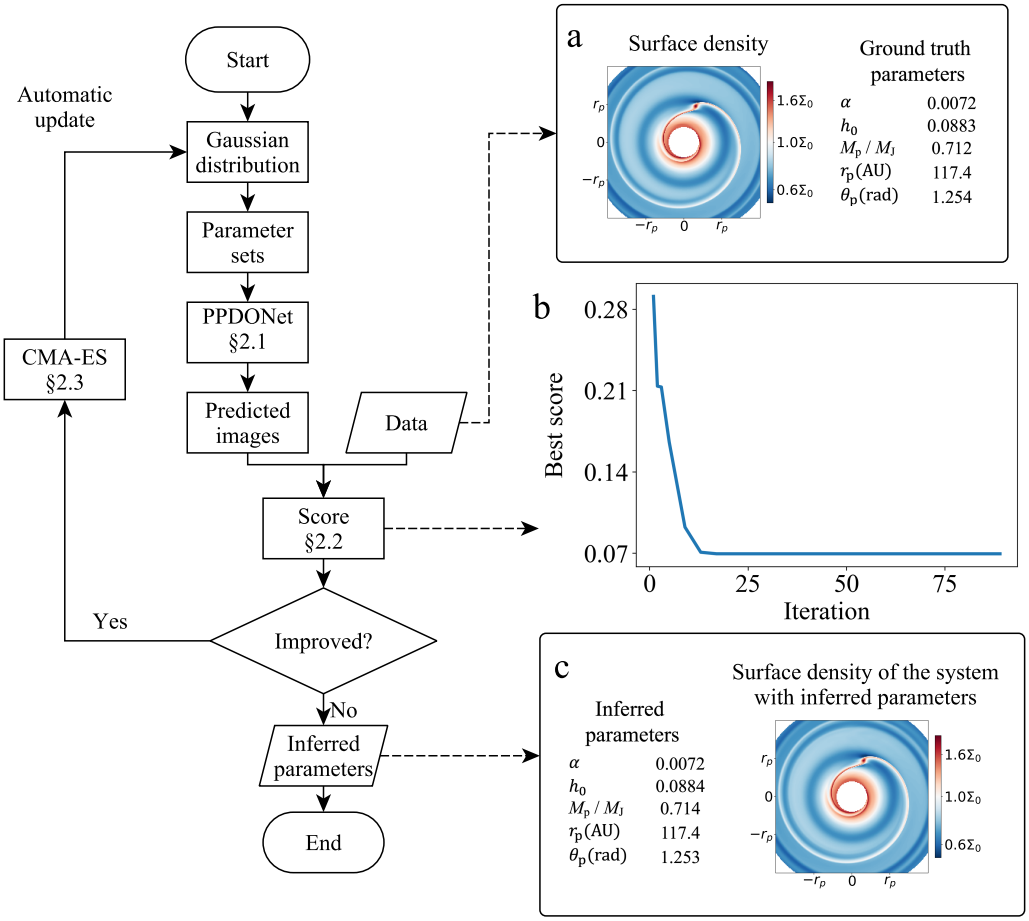

Figure 3.1: A flow chart illustrating the iterative parameter update procedure in Disk2Planet inverse problem solver. The solver iterates a 5D Gaussian distribution representing the most probable parameters (α, h_0, q, r_p, θ_p) that result in the minimal difference between the model and the input data. At each iteration, the Gaussian distribution is refined by testing 128 sets of parameters sampled from the current distribution. These parameters are processed by the ML-based solver PPDONet (§3.1.1) to predict the corresponding disk maps. Differences between these maps and the data are quantified by the score (§3.1.2). The CMA–ES optimizer (§3.1.3) updates the Gaussian distribution to converge towards parameter sets with smaller scores. This process iterates until the distribution converges to the optimal parameters. On the right, I show an example of the inference process: (a) the input surface density map and its true parameters; (b) the evolution of the best score over iterations; (c) the inferred parameters and the corresponding surface density solution.

estimate and is initially set to 0.01 [1]. Each iteration includes four steps:

1. Sample 128 sets of parameters from the Gaussian distribution;

[1]See the instructions at `https://CMA--ES.github.io/cmaes_sourcecode_page.html`.

2. Predict the disk model for each parameter set using the fast machine learning-based forward problem solver PPDONet (§3.1.1);

3. Assign a score to each prediction to quantify how well it matches the input data (§3.1.2);

4. Update the Gaussian distribution's mean and standard deviation based on the scores using the Covariance Matrix Adaptation Evolution Strategy (CMA–ES; §3.1.3).

The iterative process is repeated until the score in step (3) can no longer be minimized, indicating that the best possible set of parameters has been found.

Figure 3.1 illustrates how the tool works. The input data (panel a) contains a surface density map generated using the FARGO3D code [Masset, 2000, Benítez-Llambay and Masset, 2016] with its true parameters listed on the side. The evolution of the score is shown in panel b. The inferred (optimal) parameters are shown in panel c, where I achieve sub–percentage level accuracy for all five parameters. Panel (c) also shows the surface density map corresponding to the inferred parameters, obtained using PPDONet, enabling visual inspection.

3.1.1 The PPDONet-based Forward Problem Solver

For each set of (α, h_0, q) sampled during iterations, I use the fast forward problem solver PPDONet [Mao et al., 2023] to predict surface density Σ, radial velocity v_r, and azimuthal velocity v_θ maps, each computed in one hundredth of a second on an Nvidia A100 chip. Line-of-sight velocity maps $v_\mathrm{LOS} = v_r \cos(\theta) - v_\theta \sin(\theta)$ can be synthesized in post-processing. These maps are then rotated and stretched according to the planet location (r_p, θ_p) in the current sample. PPDONet is a publicly available machine learning tool[2] that efficiently maps scalar parameters from partial differential equations to their solutions. As demonstrated in Mao et al. [2023, Fig. 2], the predicted disk maps are visually indistinguishable from FARGO3D simulations within the parameter space of interest defined earlier.

[2] `https://github.com/smao-astro/PPDONet`

3.1.2 The Score for Data-Output Comparisons

The PPDONet–predicted disk map for each sampled parameter set is compared with the corresponding input data to generate a score quantifying their differences. For velocities, the score is the relative L_2 error:

$$L_2(\text{velocity}) = \|\text{pred} - \text{data}\|_2 / \|\text{data}\|_2, \tag{3.1}$$

where $\|\cdot\|_2$ denotes the root mean square over all pixel values. For surface density, the score is the logarithmic relative L_2 error (e.g. Zhang et al. 2022)

$$L_2(\Sigma) = \|\log_{10}\text{pred} - \log_{10}\text{data}\|_2 / \|\log_{10}\text{data}\|_2. \tag{3.2}$$

The score is designed to handle the data complications illustrated in Fig. 3.2. For noisy data (block A), L_2 is directly computed between the noisy data and the noise–free predicted model. For data with missing parts (block B), the error calculation is confined to valid pixels only. If the data includes multiple components, such as Σ and $v_{\rm LOS}$ (block C), L_2 for each component are averaged to produce a composite measure.

3.1.3 The Optimization Algorithm CMA–ES

The Covariance Matrix Adaptation Evolution Strategy (CMA–ES) automatically updates the mean and covariance matrix of the Gaussian distribution to minimize the scores (§3.1.2) of the parameters sampled from the Gaussian distribution over iterations. CMA–ES is designed for scenarios where the correlation between models and scores is complex and not well understood analytically.

Each update in CMA–ES follows an adaptive strategy similar to that found in evolutionary biology: The algorithm ranks parameter sets by their scores, selecting the lowest half as "parents". It then blends these parent sets through recombination and mutation to calculate the mean and covariance matrix for the new Gaussian distribution. This new Gaussian reflects the most successful parameter combinations at that moment, guiding the search towards promising directions. The updated Gaussian is then employed to generate "children" parameter sets for the next iteration. This iterative process repeats until the score improvement plateaus, indicating that the optimal parameters have been effectively identified by the latest Gaussian distribution.

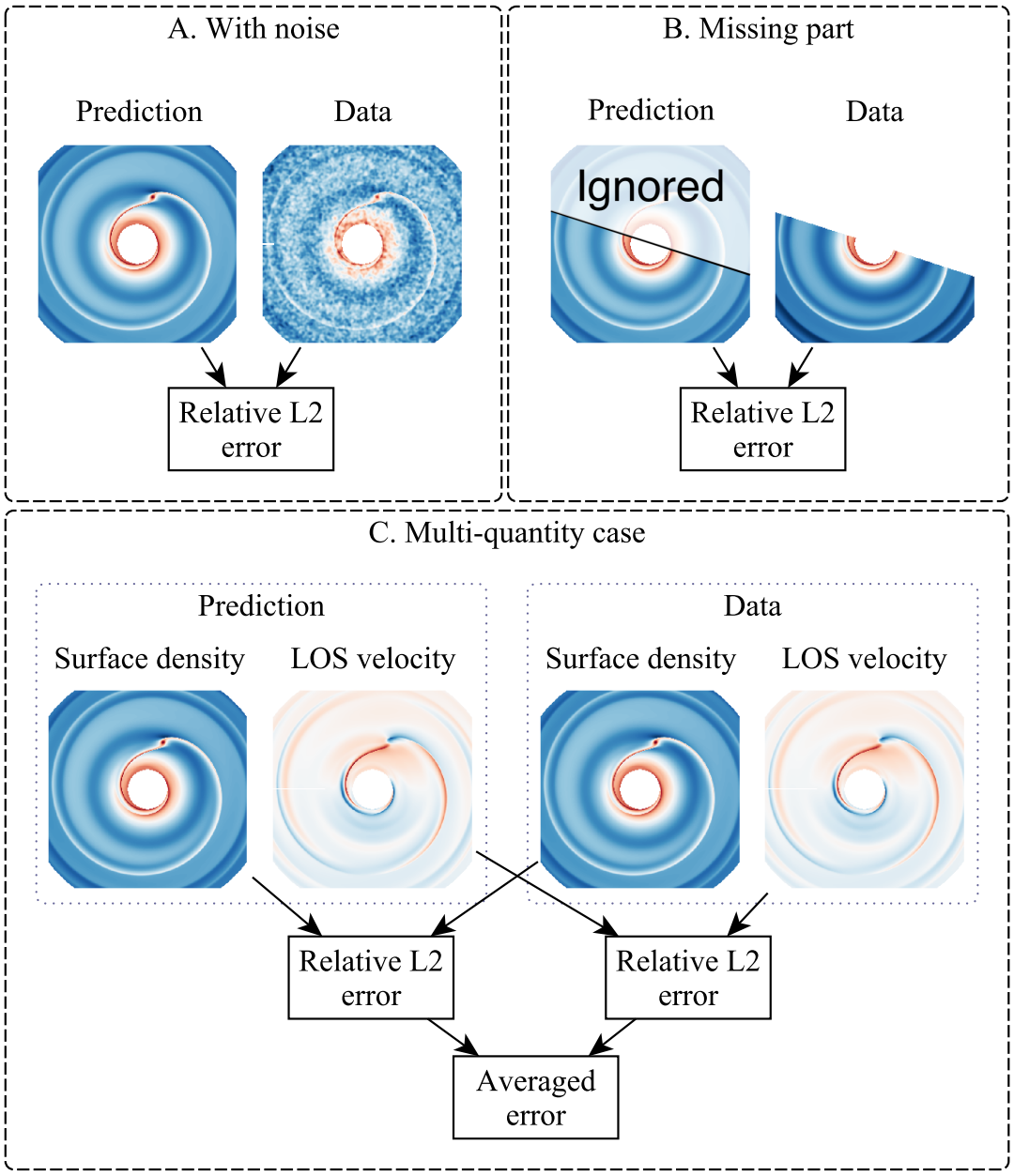

Figure 3.2: Score calculation for three cases of input data. Block A: For noisy input data, the score is calculated the same way as for noise–free data. Block B: For input data with missing areas, only the available pixels are used. Block C: For input data containing multiple quantities, the error for each quantity is calculated, and then the average of all errors is taken as the score.

3.2 Performance

In this section, I evaluate the parameter inference accuracy of Disk2Planet. I begin with the baseline case in which the input data contains a complete noise-free map of

surface density (§3.2.1). I then test cases in which the input data contains multiple physical quantities (§3.2.2), noises (§3.2.3), and missing parts (§3.2.4).

3.2.1 The baseline case — input data with surface density only

Fig. 3.3 shows the inferred versus ground truth planet masses for 256 tests uniformly sampled from the parameter space specified in Mao et al. [2023, Table 1]. Overall, the two agree well. The agreement can be quantitatively assessed using the $r2$-score:

$$r2 = 1 - SS(M_{\rm p}^{\rm inferred} - M_{\rm p}^{\rm true})/SS(M_{\rm p}^{\rm true} - \overline{M_{\rm p}^{\rm true}}), \tag{3.3}$$

where SS denotes the sum of square of all cases and $\overline{M_{\rm p}^{\rm true}}$ is the mean of all ground truth values. An $r2$-score close to one indicates near-perfect agreement. Our tool achieves an $r2$-score of 0.9994. For comparison, CNN-based parameter inference typically achieves $r2$-scores of 0.97 to 0.98 (Auddy et al. 2021, Fig. 4; Ruzza et al. 2024, Fig. 5).

Another metric for assessing the tool's performance is the error distribution of each parameter, as done by Zhang et al. [2022] and Ruzza et al. [2024]. In each test, I quantify the error in each inferred parameter as:

$$\begin{aligned}
{\rm Err}(\alpha) &= \log_{10}(\alpha^{\rm inferred}) - \log_{10}(\alpha^{\rm true}), && \text{(3.4a)}\\
{\rm Err}(h_0) &= (h_0^{\rm inferred} - h_0^{\rm true})/h_0^{\rm true}, && \text{(3.4b)}\\
{\rm Err}(q) &= \log_{10}(q^{\rm inferred}) - \log_{10}(q^{\rm true}), && \text{(3.4c)}\\
{\rm Err}(r_{\rm p}) &= (r_{\rm p}^{\rm inferred} - r_{\rm p}^{\rm true})/r_{\rm p}^{\rm true}, && \text{(3.4d)}\\
{\rm Err}(\theta_{\rm p}) &= \theta_{\rm p}^{\rm inferred} - \theta_{\rm p}^{\rm true}. && \text{(3.4e)}
\end{aligned}$$

The errors for α and q are calculated on a logarithmic scale due to their wide range across several orders of magnitude [Ruzza et al., 2024, Eq. 13]. The errors for h_0 and $r_{\rm p}$ are normalized. I then define the inference uncertainty σ as half the difference between the error distribution's $84^{\rm th}$ and $16^{\rm th}$ percentiles, and list them in the first column in Fig. 3.4: $\sigma(\alpha) = 0.022$, $\sigma(h_0) = 0.0015$, $\sigma(q) = 0.0073$, $\sigma(r_{\rm p}) = 0.00047$, $\sigma(\theta_{\rm p}) = 0.0018$. In comparison, CNN-based parameter inference achieves $\sigma(q) = 0.16$ [Zhang et al., 2022] and 0.13 [Ruzza et al., 2024], and $\sigma(\alpha) = 0.23$ [Zhang et al., 2022].

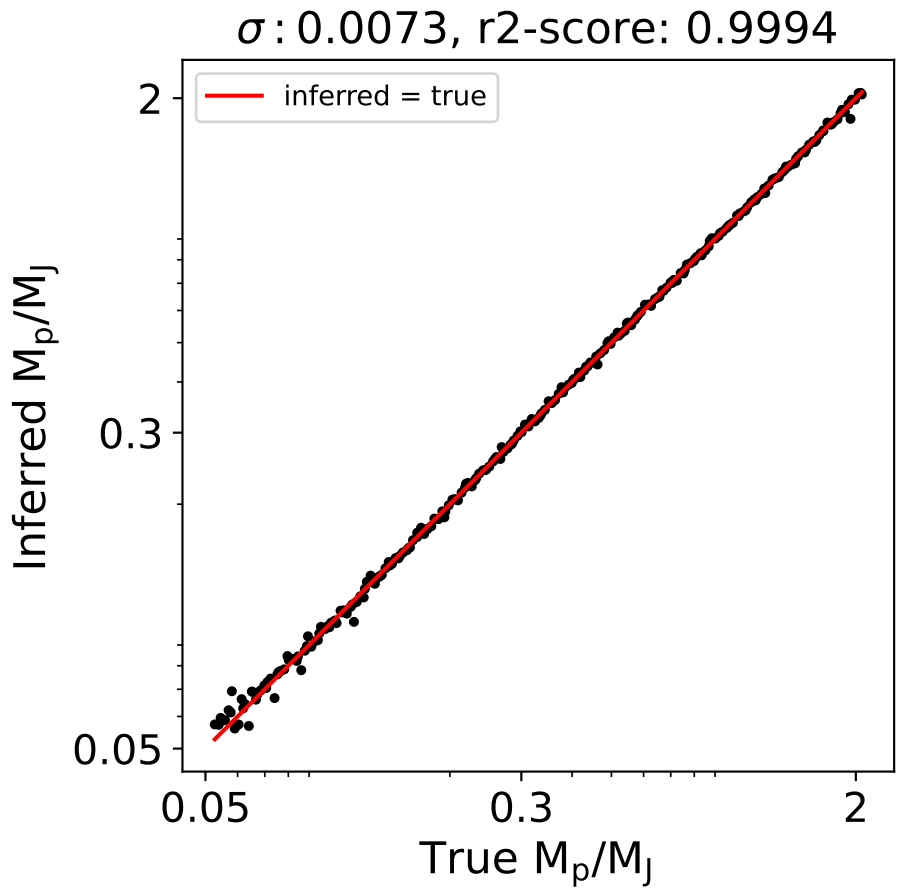

Figure 3.3: Ground truth and inferred planet masses in 256 tests using full noise–free maps of surface density as input. The tests achieve an $r2$-score (Eq. 3.3) of 0.9994 and an inference uncertainty σ of 0.0073, indicating near-perfect agreement (red solid line). See §3.2.1 for details.

I examine the error distributions and possible correlations in the multi–dimensional parameter space in Fig. 3.5a. The histograms on the diagonal show the distributions of individual parameters while the off-diagonal panels highlight pairwise correlations. Notably, all distributions are centered, indicating little systematic bias in the inferred parameters. Additionally, only two pairwise correlations (out of a total of $C(5,2) = 10$) are not isotropic: Err(α) *vs* Err(q) exhibits a positive correlation, echoing Zhang et al. [2022, Fig. 5], while Err(r_p) is negatively correlated with Err(θ_p).

	Baseline §3.1	Multiple Quantities §3.2		With Noise §3.3		Missing Parts §3.4	
Testing Datasets	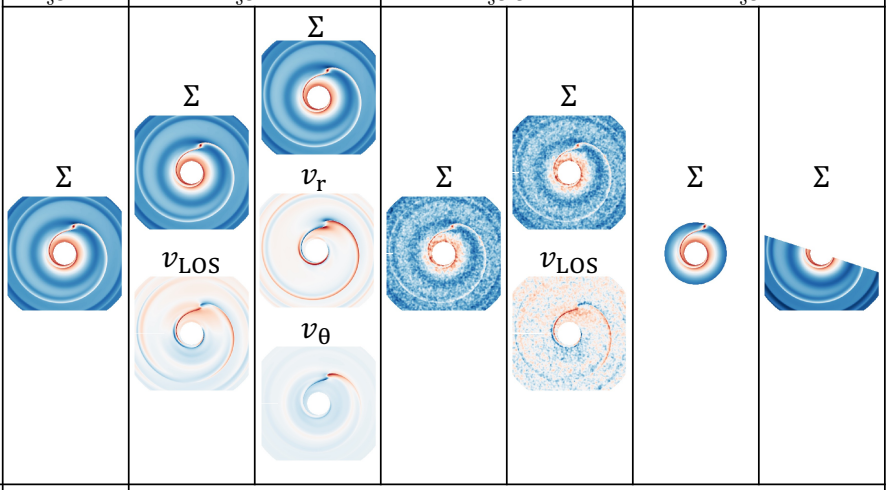						
Error	$\sigma_{baseline}$	$\sigma/\sigma_{baseline}$					
α	0.022	0.6	0.6	2.6	1.6	1.03	1.2
h_0	0.0015	0.6	0.5	3.7	1.6	4.3	1.8
q	0.0073	0.5	0.5	3.5	1.7	1.7	1.4
r_p	0.00047	0.7	0.6	3.6	1.4	6.0	3.4
θ_p	0.0018	0.97	0.8	2.7	1.8	1.7	9.0

Figure 3.4: Representative examples of the inverse problem with different types of input datasets, and the corresponding parameter inference uncertainties (σ). The input datasets contain images of, from left to right, Σ (a), Σ+$v_{\rm LOS}$ (b), Σ+$v_{\rm r}$+v_θ (c), Σ with noise (d), Σ+$v_{\rm LOS}$ with noise (e), radially cropped Σ (f), and azimuthally cropped Σ (g). 256 tests are run for each. The uncertainties are calculated as half the difference between the error distribution's $84^{\rm th}$ and $16^{\rm th}$ percentiles.

3.2.2 Input data with multiple quantities

Disk2Planet can incorporate surface density Σ, radial velocity $v_{\rm r}$, and azimuthal velocity v_θ in any combination. For example, I can supply two maps, Σ + $v_{\rm LOS}$, as illustrated in Fig. 3.4 (case (b)). This scenario mimics real situations where gas line emission observations (e.g., Zhang et al. 2021) provide these quantities. As the amount of information in the input data increases, the parameter inference accuracy improves, resulting in smaller errors. Compared to the baseline case (a), adding $v_{\rm LOS}$ reduces uncertainties for the five inferred parameters by 3% to 47% in 256 tests. Additionally, supplying three maps, Σ + $v_{\rm r}$ + v_θ, as input data (case c) further reduces uncertainties since $v_{\rm r}$ + v_θ provide more information than $v_{\rm LOS}$.

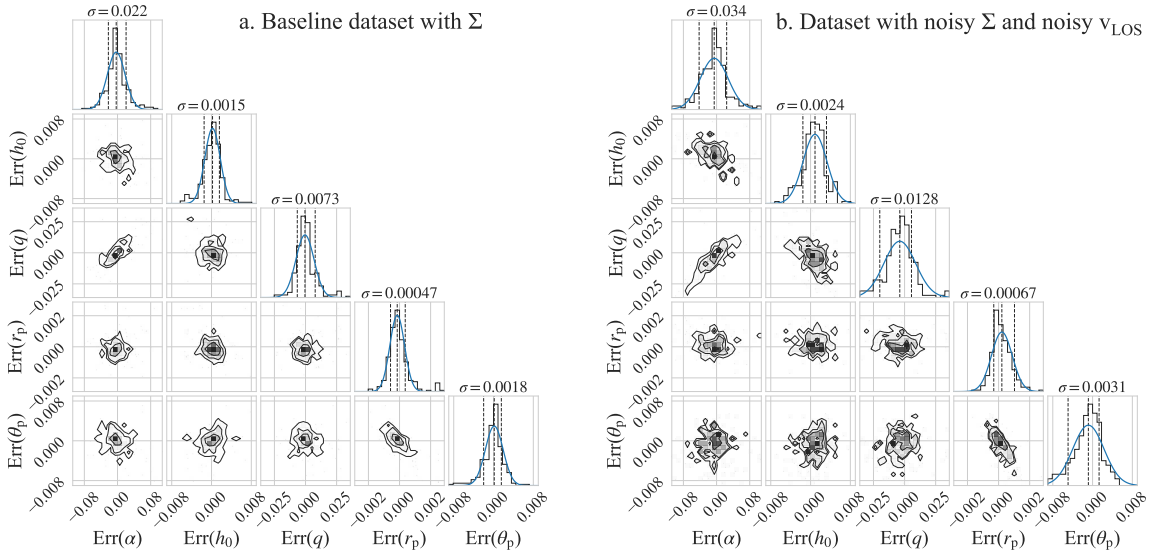

Figure 3.5: Corner plots showing the distribution of errors in the inferred parameters (Eq. 3.4). Corresponding panels on the two sides are on the same scales. The histograms on the diagonal show the distributions of individual parameters, while the off-diagonal panels highlight pairwise correlations. See §3.2.1 for details.

3.2.3 Input data with noise

Observational data often contain noise. Our inverse problem solver can handle noisy input data, as shown in cases (d) and (e) in Fig. 3.4. They are created by introducing random uniform noises in Σ (case (d)) and $\Sigma + v_{\rm LOS}$ (case (e)). The noises have a spatial scale of 2.5 AU (Zhang et al. 2018, §2.3; equivalent to 0.018 arcsec at 140 pc), added to the logarithmic pixel values with a standard deviation $0.6\times$ the average of the quantity. The resulting uncertainties for the five parameters in both cases are $2-4\times$ those in the corresponding noise–free inputs (cases (a) and (b)). The associated multi–dimensional error distributions are shown in Fig. 3.5b, with trends similar to those in the baseline case (Fig. 3.5a; §3.2.1).

3.2.4 Input data with missing parts

In observations, signals in certain regions may be missing or masked for various reasons, such as foreground extinction [Bruderer et al., 2014, Tsukagoshi et al., 2019]. Figure 3.4 illustrates two such cases: the Σ map is cropped radially beyond $1.1r_{\rm p}$ (f) and azimuthally in half (g; the planet is in the cropped region). In both scenarios, the tool performs parameter inference in all 256 tests, albeit with uncertainties $1-9\times$

those in the baseline case with a full Σ map (a). This is expected, as cropping reduces the amount of information in the input image. In the radial cropping case, $\sigma(h_0)$ and $\sigma(r_\mathrm{p})$ have the largest increases (4.3× and 6.0×, respectively), although their absolute values remain low (0.007 and 0.003, respectively). In the azimuthal cropping case, a 9–fold increase in $\sigma(\theta_\mathrm{p})$ stands out among the five uncertainties, attributed to the loss of substructures near the planet, crucial for its accurate localization. The absolute value of $\sigma(\theta_\mathrm{p})$, 0.016 (1°, or 1.6 AU for a planet at 100 AU), remains smaller than the typical resolution achieved in today's high–resolution imaging observations of disks [e.g., Benisty et al., 2022].

3.3 Advantages over existing inverse problem solvers

Disk2Planet is robust against noisy data (3.2.3). This is due to my advanced inference mechanism, which finds optimal parameters that minimize the difference between predicted disk maps and input data. Random noise does not alter the intrinsic pattern in the input data; it merely adds an unbiased random component to the difference between predicted disk maps and input data. In contrast, CNN-based methods [Auddy et al., 2021, Zhang et al., 2022, Ruzza et al., 2024], which rely heavily on local pixel values, induce significantly larger errors when signal–to–noise ratio is below ten (e.g., a planet mass error of 0.68 dex versus 0.13 dex; Ruzza et al. 2024, §5.3).

Our inverse problem solver can process incomplete images with missing parts in arbitrary shapes in a straightforward manner. As illustrated in Fig. 3.2 (Block B), the missing parts are ignored and do not contribute to the parameter inference. In contrast, CNN-based methods require completed images, as every pixel contributes to the convolution, which is key to CNNs in extracting information. In theory, CNNs can also be trained with datasets that have the same missing parts as the real observations. However, this is impractical in real–life applications, because it is often difficult to predict which parts of the image will be missing in real observations, and the missing parts can vary between observations.

Our inverse problem solver works with input images of any spatial resolution since the entire procedure is resolution–independent. In contrast, CNN–based solvers are often trained on datasets with fixed resolutions. To minimize training costs, low resolutions are typically used, such as 64×64 in Zhang et al. [2022] or 128×128 in Ruzza et al. [2024], which can degrade detailed disk substructures like spiral arms. Additionally, due to limitations in the training sets, CNN-based tools can only operate

properly when the input images have the same resolution as the training sets; if not, regridding is needed, which may result in a loss of information.

Disk2Planet locates planets by matching their induced substructures with those in the data. This contrasts with CNN-based approaches [e.g., Ruzza et al., 2024], which requires users to provide prior knowledge of the planet's location. Augmenting the training dataset in PPDONet to accommodate different planet locations is not needed neither, in contrast to CNN-based approach (e.g. Zhang et al. 2022).

3.4 Conclusions and future perspectives

I have developed a fast and fully automated inverse problem solver, Disk2Planet, capable of inferring five parameters — the Shakura–Sunyaev viscosity (α), disk aspect ratio (h_0), planet–star mass ratio (q), and the planet's radius and azimuth — from 2D steady–state disk–planet systems. Inferring these parameters from surface density in one system takes three GPU minutes on an Nvidia A100 machine. Our solver requires minimal human intervention and is user–friendly for newcomers without prior experience in numerical simulations of disk–planet interactions.

The architecture of the solver and an example application are shown in Fig. 3.1. The solver is built on the machine learning tool PPDONet, which predicts the disk maps created by a planet [Mao et al., 2023]. It employs the evolutionary optimization algorithm CMA–ES [Hansen, 2006, 2009, Hansen et al., 2010, 2019], which samples parameters from a 5D Gaussian distribution in each iteration and refines the distribution by minimizing the difference between the model and the input data.

The inputs to the solver consist of 2D maps of gas surface density and velocities in a disk. The solver can handle data with unknown noise levels, incomplete data with missing parts, and user-defined combinations of quantities (Fig. 3.4). It achieves percentage–level or smaller errors in the inferred parameters in the tests performed in this work (Fig. 3.3), representing at least an order of magnitude improvement over previous tools based on Convolutional Neural Networks [e.g., Auddy et al., 2021, Zhang et al., 2022, Ruzza et al., 2024]. As expected, the errors decrease as more information is provided by the input data.

The inverse problem solver may be improved in several ways. The current version is designed to work with 2D maps of gas surface density and velocities derived from observations [e.g., Zhang et al., 2021], rather than directly from observational data. To achieve this, an additional step is required after "Predicted images" in Fig. 3.1 to

translate these maps into synthetic observations with appropriate viewing angles. For the tool to work with maps of dust distributions obtained from millimeter continuum emission observations, a training dataset generated from gas+dust simulations will be needed to train PPDONet. This can be accomplished with minimal modifications to PPDONet and the architecture of my inverse problem solver once the training sets are produced.

Bibliography

Sean M Andrews. Observations of protoplanetary disk structures. *Annual Review of Astronomy and Astrophysics*, 58:483–528, 2020.

Sayantan Auddy, Ramit Dey, Min-Kai Lin, and Cassandra Hall. Dpnnet-2.0. i. finding hidden planets from simulated images of protoplanetary disk gaps. *The Astrophysical Journal*, 920(1):3, 2021.

Jaehan Bae and Zhaohuan Zhu. Planet-driven spiral arms in protoplanetary disks. i. formation mechanism. *The Astrophysical Journal*, 859(2):118, 2018.

Myriam Benisty, Carsten Dominik, Katherine Follette, Antonio Garufi, Christian Ginski, Jun Hashimoto, Miriam Keppler, Willy Kley, and John Monnier. Optical and near-infrared view of planet-forming disks and protoplanets. *arXiv preprint arXiv:2203.09991*, 2022.

Pablo Benítez-Llambay and Frédéric S Masset. Fargo3d: a new gpu-oriented mhd code. *The Astrophysical Journal Supplement Series*, 223(1):11, 2016.

Simon Bruderer, Nienke van der Marel, Ewine F Van Dishoeck, and Tim A van Kempen. Gas structure inside dust cavities of transition disks: Ophiuchus irs 48 observed by alma. *Astronomy & Astrophysics/Astronomie et Astrophysique*, 562, 2014.

Valentin Christiaens, Simon Casassus, Olivier Absil, Faustine Cantalloube, C Gomez Gonzalez, J Girard, R Ramírez, B Pairet, V Salinas, Daniel J Price, et al. Separating extended disc features from the protoplanet in pds 70 using vlt/sinfoni. *Monthly Notices of the Royal Astronomical Society*, 486(4):5819–5837, 2019.

Marco Cilibrasi, Mario Flock, and Judit Szulágyi. Meridional circulation driven by planetary spiral wakes in radiative and magnetized protoplanetary discs. *Monthly Notices of the Royal Astronomical Society*, 523(2):2039–2058, 2023.

Thayne Currie, Kellen Lawson, Glenn Schneider, Wladimir Lyra, John Wisniewski, Carol Grady, Olivier Guyon, Motohide Tamura, Takayuki Kotani, Hajime Kawahara, et al. Images of embedded jovian planet formation at a wide separation around ab aurigae. *Nature Astronomy*, 6(6):751–759, 2022.

Giovanni Dipierro and Guillaume Laibe. An opening criterion for dust gaps in protoplanetary discs. *Monthly Notices of the Royal Astronomical Society*, 469(2):1932–1948, 2017.

Giovanni Dipierro, Daniel Price, Guillaume Laibe, Kieran Hirsh, Alice Cerioli, and Giuseppe Lodato. On planet formation in hl tau. *Monthly Notices of the Royal Astronomical Society: Letters*, 453(1):L73–L77, 2015.

Ruobing Dong and Jeffrey Fung. How bright are planet-induced spiral arms in scattered light? *The Astrophysical Journal*, 835(1):38, 2017.

Ruobing Dong, Zhaohuan Zhu, Roman R Rafikov, and James M Stone. Observational signatures of planets in protoplanetary disks: Spiral arms observed in scattered light imaging can be induced by planets. *The Astrophysical Journal Letters*, 809(1):L5, 2015a.

Ruobing Dong, Zhaohuan Zhu, and Barbara Whitney. Observational signatures of planets in protoplanetary disks. i. gaps opened by single and multiple young planets in disks. *The Astrophysical Journal*, 809(1):93, 2015b.

Ruobing Dong, Shengtai Li, Eugene Chiang, and Hui Li. Multiple disk gaps and rings generated by a single super-earth. ii. spacings, depths, and number of gaps, with application to real systems. *The Astrophysical Journal*, 866(2):110, 2018.

Jeffrey Fung, Ji-Ming Shi, and Eugene Chiang. How empty are disk gaps opened by giant planets? *The Astrophysical Journal*, 782(2):88, 2014.

Xavier Glorot and Yoshua Bengio. Understanding the difficulty of training deep feedforward neural networks. In *Proceedings of the thirteenth international conference on artificial intelligence and statistics*, pages 249–256. JMLR Workshop and Conference Proceedings, 2010.

Raghav Gnanasambandam, Bo Shen, Jihoon Chung, Xubo Yue, et al. Self-scalable tanh (stan): Faster convergence and better generalization in physics-informed neural networks. *arXiv preprint arXiv:2204.12589*, 2022.

SY Haffert, AJ Bohn, J De Boer, IAG Snellen, J Brinchmann, JH Girard, CU Keller, and R Bacon. Two accreting protoplanets around the young star pds 70. *Nature Astronomy*, 3(8):749–754, 2019.

Nikolaus Hansen. Compilation of results on the 2005 cec benchmark function set. *Online, May*, 2006.

Nikolaus Hansen. Benchmarking a bi-population cma-es on the bbob-2009 noisy testbed. In *Proceedings of the 11th Annual Conference Companion on Genetic and Evolutionary Computation Conference: Late Breaking Papers*, pages 2397–2402, 2009.

Nikolaus Hansen, Anne Auger, Raymond Ros, Steffen Finck, and Petr Pošík. Comparing results of 31 algorithms from the black-box optimization benchmarking bbob-2009. In *Proceedings of the 12th annual conference companion on Genetic and evolutionary computation*, pages 1689–1696, 2010.

Nikolaus Hansen, Youhei Akimoto, and Petr Baudis. CMA-ES/pycma on Github. Zenodo, DOI:10.5281/zenodo.2559634, February 2019. URL `https://doi.org/10.5281/zenodo.2559634`.

Jun Hashimoto, Yuhiko Aoyama, Mihoko Konishi, Taichi Uyama, Shinsuke Takasao, Masahiro Ikoma, and Takayuki Tanigawa. Accretion properties of pds 70b with muse. *The Astronomical Journal*, 159(5):222, 2020.

Andres F Izquierdo, Leonardo Testi, Stefano Facchini, Giovanni P Rosotti, and Ewine F van Dishoeck. The disc miner i: A statistical framework to detect and quantify kinematical perturbations driven by young planets in discs. *arXiv preprint arXiv:2104.09596*, 2021.

Sheng Jin, Shengtai Li, Andrea Isella, Hui Li, and Jianghui Ji. Modeling dust emission of hl tau disk based on planet–disk interactions. *The Astrophysical Journal*, 818 (1):76, 2016.

Kazuhiro D Kanagawa, Takayuki Muto, Hidekazu Tanaka, Takayuki Tanigawa, Taku Takeuchi, Takashi Tsukagoshi, and Munetake Momose. Mass constraint for a planet in a protoplanetary disk from the gap width. *Publications of the Astronomical Society of Japan*, 68(3):43, 2016.

Miriam Keppler, Myriam Benisty, André Müller, Th Henning, R Van Boekel, F Cantalloube, C Ginski, RG Van Holstein, A-L Maire, A Pohl, et al. Discovery of a planetary-mass companion within the gap of the transition disk around pds 70. *Astronomy & Astrophysics*, 617:A44, 2018.

Diederik P Kingma and Jimmy Ba. Adam: A method for stochastic optimization. *arXiv preprint arXiv:1412.6980*, 2014.

Zewen Li, Fan Liu, Wenjie Yang, Shouheng Peng, and Jun Zhou. A survey of convolutional neural networks: analysis, applications, and prospects. *IEEE transactions on neural networks and learning systems*, 2021.

Lu Lu, Pengzhan Jin, Guofei Pang, Zhongqiang Zhang, and George Em Karniadakis. Learning nonlinear operators via deeponet based on the universal approximation theorem of operators. *Nature Machine Intelligence*, 3(3):218–229, 2021.

Shunyuan Mao. Ppdonet: Deep operator networks for fast prediction of steady-state solutions in disk-planet systems, 2023. URL `https://zenodo.org/record/7888957`.

Shunyuan Mao, Ruobing Dong, Lu Lu, Kwang Moo Yi, Sifan Wang, and Paris Perdikaris. Ppdonet: Deep operator networks for fast prediction of steady-state solutions in disk–planet systems. *The Astrophysical Journal Letters*, 950(2):L12, 2023.

F Masset. Fargo: A fast eulerian transport algorithm for differentially rotating disks. *Astronomy and Astrophysics Supplement Series*, 141(1):165–173, 2000.

Ryan Miranda and Roman R Rafikov. Gaps and rings in protoplanetary disks with realistic thermodynamics: The critical role of in-plane radiation transport. *The Astrophysical Journal*, 904(2):121, 2020.

André Müller, Miriam Keppler, Th Henning, Matthias Samland, Gael Chauvin, Hervé Beust, A-L Maire, Karan Molaverdikhani, Roy van Boekel, Myriam Benisty, et al.

Orbital and atmospheric characterization of the planet within the gap of the pds 70 transition disk. *Astronomy & Astrophysics*, 617:L2, 2018.

Keiron O'Shea and Ryan Nash. An introduction to convolutional neural networks. *arXiv preprint arXiv:1511.08458*, 2015.

S-J Paardekooper and Garrelt Mellema. Dust flow in gas disks in the presence of embedded planets. *arXiv preprint astro-ph/0603132*, 2006.

Sijme-Jan Paardekooper, Ruobing Dong, Paul Duffell, Jeffrey Fung, Frederic S Masset, Gordon Ogilvie, and Hidekazu Tanaka. Planet-disk interactions. *arXiv preprint arXiv:2203.09595*, 2022.

C Pinte, G van Der Plas, F Ménard, DJ Price, V Christiaens, T Hill, D Mentiplay, C Ginski, E Choquet, Y Boehler, et al. Kinematic detection of a planet carving a gap in a protoplanetary disk. *Nature Astronomy*, 3(12):1109–1114, 2019.

Christophe Pinte, DJ Price, F Ménard, G Duchêne, WRF Dent, Tracey Hill, I de Gregorio-Monsalvo, A Hales, and D Mentiplay. Kinematic evidence for an embedded protoplanet in a circumstellar disk. *The Astrophysical Journal Letters*, 860(1):L13, 2018.

Ian Rabago and Zhaohuan Zhu. Constraining protoplanetary disc accretion and young planets using alma kinematic observations. *Monthly Notices of the Royal Astronomical Society*, 502(4):5325–5339, 2021.

Giovanni P Rosotti, Attila Juhasz, Richard A Booth, and Cathie J Clarke. The minimum mass of detectable planets in protoplanetary discs and the derivation of planetary masses from high-resolution observations. *Monthly Notices of the Royal Astronomical Society*, 459(3):2790–2805, 2016.

Alessandro Ruzza, Giuseppe Lodato, and Giovanni Pietro Rosotti. Dbnets: A publicly available deep learning tool to measure the masses of young planets in dusty protoplanetary discs. *arXiv preprint arXiv:2402.12448*, 2024.

Il'ya Meerovich Sobol'. On the distribution of points in a cube and the approximate evaluation of integrals. *Zhurnal Vychislitel'noi Matematiki i Matematicheskoi Fiziki*, 7(4):784–802, 1967.

Richard Teague, Jaehan Bae, Edwin A Bergin, Tilman Birnstiel, and Daniel Foreman-Mackey. A kinematical detection of two embedded jupiter-mass planets in hd 163296. *The Astrophysical Journal Letters*, 860(1):L12, 2018.

JP Terry, Cassandra Hall, Sean Abreau, and Sergei Gleyzer. Locating hidden exoplanets in alma data using machine learning. *The Astrophysical Journal*, 941(2): 192, 2022.

Takashi Tsukagoshi, Munetake Momose, Yoshimi Kitamura, Masao Saito, Ryohei Kawabe, Sean Andrews, David Wilner, Tomoyuki Kudo, Jun Hashimoto, Nagayoshi Ohashi, et al. The flared gas structure of the transitional disk around sz 91. *The Astrophysical Journal*, 871(1):5, 2019.

Kevin Wagner, Katherine B Follette, Laird M Close, Dániel Apai, Aidan Gibbs, Miriam Keppler, André Müller, Thomas Henning, Markus Kasper, Ya-Lin Wu, et al. Magellan adaptive optics imaging of pds 70: measuring the mass accretion rate of a young giant planet within a gapped disk. *The Astrophysical Journal Letters*, 863(1):L8, 2018.

Jason J Wang, Sivan Ginzburg, Bin Ren, Nicole Wallack, Peter Gao, Dimitri Mawet, Charlotte Z Bond, Sylvain Cetre, Peter Wizinowich, Robert J De Rosa, et al. Keck/nirc2 l'-band imaging of jovian-mass accreting protoplanets around pds 70. *The Astronomical Journal*, 159(6):263, 2020.

Chenxi Wu, Min Zhu, Qinyang Tan, Yadhu Kartha, and Lu Lu. A comprehensive study of non-adaptive and residual-based adaptive sampling for physics-informed neural networks. *Computer Methods in Applied Mechanics and Engineering*, 403: 115671, 2023.

Han Gyeol Yun, Woong-Tae Kim, Jaehan Bae, and Cheongho Han. Properties of density and velocity gaps induced by a planet in a protoplanetary disk. *The Astrophysical Journal*, 884(2):142, 2019.

Ke Zhang, Alice S Booth, Charles J Law, Arthur D Bosman, Kamber R Schwarz, Edwin A Bergin, Karin I Öberg, Sean M Andrews, Viviana V Guzmán, Catherine Walsh, et al. Molecules with alma at planet-forming scales (maps). v. co gas distributions. *The Astrophysical Journal Supplement Series*, 257(1):5, 2021.

Shangjia Zhang, Zhaohuan Zhu, Jane Huang, Viviana V Guzmán, Sean M Andrews, Tilman Birnstiel, Cornelis P Dullemond, John M Carpenter, Andrea Isella, Laura M Pérez, et al. The disk substructures at high angular resolution project (dsharp). vii. the planet–disk interactions interpretation. *The Astrophysical Journal Letters*, 869(2):L47, 2018.

Shangjia Zhang, Zhaohuan Zhu, and Mingon Kang. Pgnets: planet mass prediction using convolutional neural networks for radio continuum observations of protoplanetary discs. *Monthly Notices of the Royal Astronomical Society*, 510(3):4473–4484, 2022.

Yifan Zhou, Aniket Sanghi, Brendan P Bowler, Ya-Lin Wu, Laird M Close, Feng Long, Kimberly Ward-Duong, Zhaohuan Zhu, Adam L Kraus, Katherine B Follette, et al. Hst/wfc3 hα direct-imaging detection of a pointlike source in the disk cavity of ab aur. *The Astrophysical Journal Letters*, 934(1):L13, 2022.

Zhaohuan Zhu, James M Stone, Roman R Rafikov, and Xue-ning Bai. Particle concentration at planet-induced gap edges and vortices. i. inviscid three-dimensional hydro disks. *The Astrophysical Journal*, 785(2):122, 2014.